Check for updates

Angewandte Chemie International Edition

Angewandte International Edition Chemie

How to cite: *Angew. Chem. Int. Ed.* **2026**, 65, e4551056
doi.org/10.1002/anie.4551056

RESEARCH ARTICLE

Proximal Symmetry-Enhanced Single-Atom Ni and In Situ Evolved Co Nanoparticle in MOFs for Synergistically Boosted Electrocatalytic Urea Synthesis

Ruichao Xu[1] | Zhenyang Dai[1] | Weizhi Gu[2] | Weiqi Lu[2] | Fengtang Zhao[2] | Lingshan Qu[1] | Jinglin Yuan[1] | Yajuan Feng[1] | Long Jiao[2] | Hai-Long Jiang[2] | Zhihu Sun[1]

[1]National Synchrotron Radiation Laboratory, University of Science and Technology of China, Hefei, P. R. China | [2]Hefei National Research Center for Physical Sciences At the Microscale, Department of Chemistry, University of Science and Technology of China, Anhui, P. R. China

Correspondence: Yajuan Feng (fengyj6@ustc.edu.cn) | Long Jiao (longjiao@ustc.edu.cn) | Zhihu Sun (zhsun@ustc.edu.cn)

Received: 14 June 2026 | **Revised:** 18 August 2026 | **Accepted:** 7 September 2026

ABSTRACT

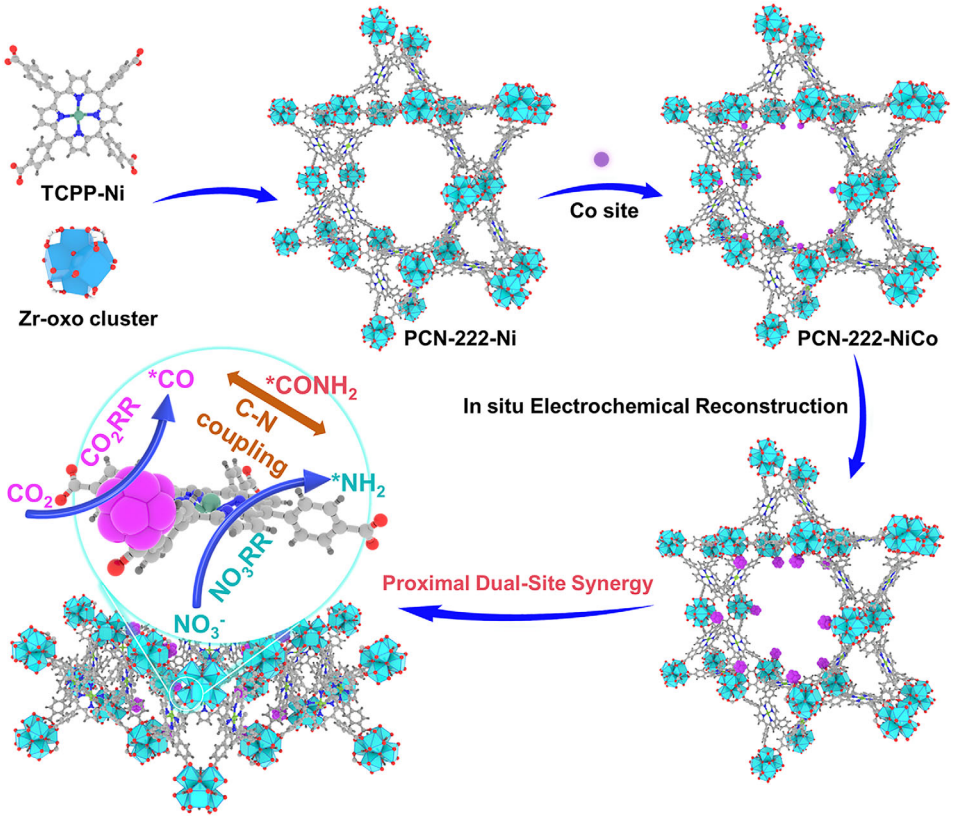
Catalysts with synergetic dual sites offer a promising way to drive efficient coupling reactions. Metal–organic frameworks (MOFs) are powerful for integrating diverse functional units, while the precise fabrication of dual sites in close proximity still remains challenging. Herein, Zr-based PCN-222-NiCo with single-atom (SA) Ni and Co precisely decorated on porphyrin ligands and Zr–oxo clusters separately is fabricated. During electrocatalysis, the SA Co sites are in situ reduced to nanoparticles (NPs) decorated on the pore wall of MOFs, which improves the planar symmetry of the Ni—N_4 sites and creates tightly coupled Co NP/SA Ni dual-sites. In the electrocatalytic C—N coupling for urea synthesis, the enhanced symmetry of Ni–N_4 lowers the *NO-to-*NOH rate-determining step barrier for NO_3^- reduction, and the in situ evolved Co NPs facilitate the *COOH-to-*CO conversion for CO_2 activation. This unique dual-site architecture minimizes the diffusion distance of *NH_2 and *CO intermediates and simultaneously facilitates the formation of the *$CONH_2$ key intermediate. PCN-222-NiCo exhibits a maximum Faradaic efficiency (FE) of 36.8% at −0.4 V vs RHE with a urea yield of 28.1 mmol h^{-1} g_{cat}^{-1}, outperforming MOFs with single-site counterparts. This work offers a strategy to build proximal synergistic dual sites for efficient coupling reactions.

1 | Introduction

Dual-site catalysts have emerged as a promising strategy for heterogeneous catalytic reactions involving multi-reactants activation and coupling pathways, such as electrocatalytic C–N coupling [1–5]. As a sustainable alternative to urea synthesis, electrocatalytic co-reduction of nitrate and CO_2 to urea can simultaneously realize nitrate pollutant degradation and CO_2 valorization under ambient conditions for high-value urea production. However, the selective C–N coupling process suffers from intrinsically sluggish kinetics due to low coupling rate, short-lived reactive intermediates and intense competition from side reactions [3, 6–9]. By integrating two distinct catalytic sites with tailored functions, dual-site architectures enable the separated activation of different reactants, facilitate intermediate coupling, and optimize the overall reaction kinetics, thereby delivering superior catalytic performance to counterparts with single catalytic sites [10–13]. Compared with conventional catalysts with single catalytic sites, dual-site configurations can effectively break the inherent limitation of single catalytic sites and enhance reaction performance toward coupled products [14–18]. Nevertheless, the rational design of high-performance catalysts with dual sites in close proximity still faces fundamental challenges, including the precise spatial positioning of dual

Ruichao Xu, Zhenyang Dai, and Weizhi Gu contributed equally to this work.

All rights reserved, including rights for text and data mining and training of artificial intelligence technologies or similar technologies.
© 2026 Wiley-VCH GmbH



SCHEME 1 | Schematic illustration of the construction of proximal SA Ni and Co NPs dual sites based on the pre-designed PCN-222-NiCo for synergistic electrocatalytic C–N coupling.

catalytic sites and the controllable electronic interaction between them [19–22].

Metal–organic frameworks (MOFs) with well-defined crystalline structures and programmable coordination environments are regarded as an ideal platform for the precise fabrication of catalytic sites [23–27]. The functionalizable ligands and metal nodes, as well as the confined pore space of MOFs, enable atomic-level precise control over the distance, spatial arrangement, and electronic interaction between dual active sites, allowing the maximization of their cooperativity [28–33]. Currently, most studies on MOF-based catalysts with dual sites mainly focus on the application of cascade reactions, which requires relatively loose control over site distance and interactions [34–43]. However, achieving atomically precise control of dual-site cooperativity to facilitate intermediate coupling remains challenging and largely unexplored.

To address this issue, a PCN-222-NiCo material with porphyrin linkers containing single-atom (SA) Ni (Ni-TCPP) and SA Co grafted onto Zr–oxo clusters is constructed (Scheme 1). In electrocatalytic C–N coupling for urea synthesis, the PCN-222-NiCo catalyst exhibits a superior urea yield of 28.1 mmol h^{-1} $g_{cat}{}^{-1}$ with a maximum Faradaic efficiency (FE) of 36.8% at −0.4 V vs. reversible hydrogen electrode (RHE), much higher than those of catalysts with only SA Ni sites on porphyrin linker or static Co NP site within MOFs. By combining in situ x-ray absorption fine structure (XAFS), high energy resolution fluorescence detected x-ray absorption near-edge structure (HERFD-XANES), in situ infrared/Raman spectroscopy characterizations, and density functional theory (DFT) calculations, it is found that the Co sites on metal nodes of PCN-222-NiCo undergo in situ reduction to form Co nanoparticles (NPs) in close proximity to Ni—N_4 sites on porphyrin ligands, which interact with SA Ni sites to enhance their planar symmetry. As a result, the in situ formed Co NPs facilitate the *CO conversion from *COOH for CO_2 activation, and the symmetry-enhanced SA Ni sites present optimized Ni 3d orbitals with a reduced *NO-to-*NOH barrier for NO_3^- reduction. Besides, this proximity of Co NPs and SA Ni, ensured by the confined space of MOF, minimizes the diffusion distance between $*NH_2$ and *CO, and accelerates the efficient formation of $*CONH_2$ key intermediate to promote urea production.

2 | Results and Discussion

A stable Zr-based MOF, named PCN-222-Ni, constructed by Ni-5,10,15,20-Tetra(4-carboxyphenyl)porphyrin (Ni-TCPP) linker and Zr–oxo cluster, was synthesized successfully according to reported literature [44–46]. The transmission electron microscopy (TEM) images of PCN-222-Ni reveal a uniform rod-like microscopic morphology (Figure S1). Subsequently, PCN-222-Ni was treated with the acetonitrile (MeCN) solution of Co^{2+} under microwave-assisted heating to decorate Co^{2+} onto coordinatively unsaturated metal nodes of PCN-222-Ni, promoting efficient Co diffusion and homogeneous ion exchange in a shorter time, yielding the PCN-222-NiCo material with well-retained crystallinity and rod-like morphology (Figure

15213773, 2026, 45, Downloaded from https://onlinelibrary.wiley.com/doi/10.1002/anie.4551056 by University Of Science, Wiley Online Library on [02/11/2026]. See the Terms and Conditions (https://onlinelibrary.wiley.com/terms-and-conditions) on Wiley Online Library for rules of use; OA articles are governed by the applicable Creative Commons License

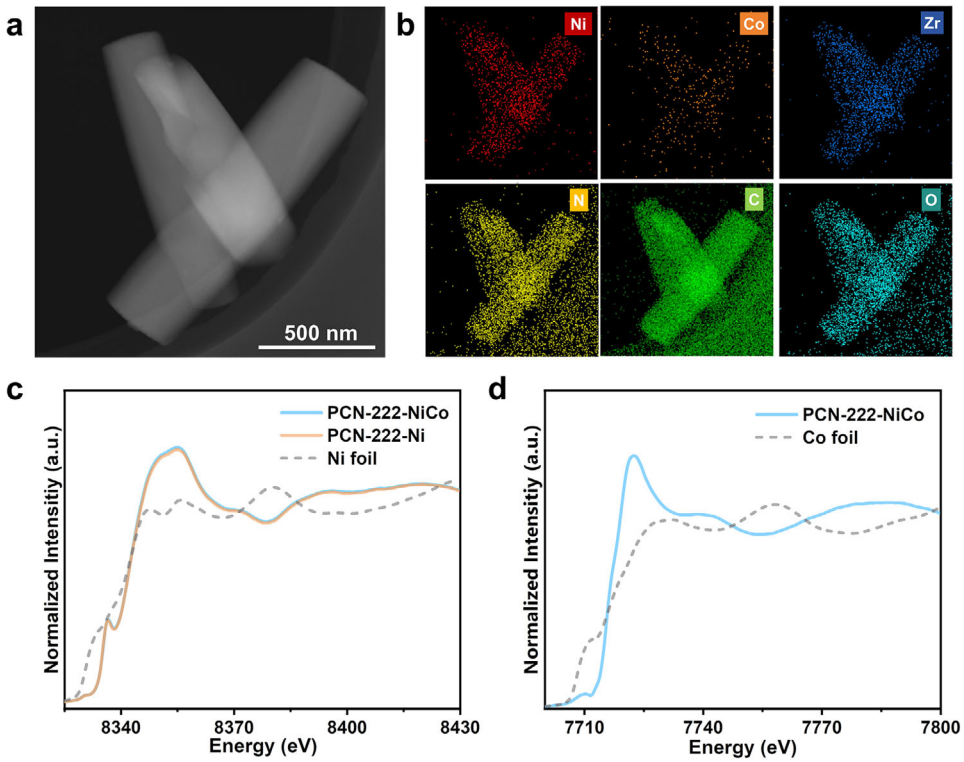


FIGURE 1 | (a) STEM image of PCN-222-NiCo and (b) corresponding elemental mapping images of Ni, Co, Zr, N, C, and O elements. (c) XANES spectra at the Ni *K*-edge of PCN-222-NiCo, PCN-222-Ni, and Ni foil. (d) XANES spectra at Co *K*-edge of PCN-222-NiCo and Co foil.

S2). Inductively coupled plasma atomic emission spectroscopy (ICP-AES) measurements confirm that the Ni and Co loadings in PCN-222-NiCo reach 1.65 and 1.28 wt%, respectively, whereas the Ni loading of PCN-222-Ni was determined to be 1.73 wt% (Table S1). No observable metal agglomeration was observed in x-ray diffraction (XRD) analysis (Figure S3). The magnified TEM image displays well-defined pore channels with a d-spacing of 3.3 nm, corresponding to the (101) crystal plane of PCN-222 (Figure S4). Both PCN-222-Ni and PCN-222-NiCo samples exhibit typical type-IV N_2 adsorption–desorption isotherms with distinct hysteresis loops, verifying their mesoporous features characteristic of porphyrin-based Zr-MOFs (Figure S5). Raman spectra of both samples retain characteristic peaks assigned to pyrrole ring and C═C bonding vibrations of the porphyrin skeleton, demonstrating the intact framework of PCN-222 MOF after metal loading (Figure S6). Fourier-transform infrared (FT-IR) spectroscopy confirms that all catalysts retain the MOF structure characteristic of PCN-based MOFs and reveals the metal–ligand coordination vibrations induced by Ni incorporation (Figure S7). Moreover, the scanning transmission electron microscopy (STEM) image (Figure 1a) and the corresponding elemental mapping images of PCN-222-NiCo demonstrate the homogeneous distribution of Ni, Co, Zr, and O elements over the entire MOF matrix (Figure 1b).

To elucidate the local electronic structure and coordination environment of Ni and Co species, XANES spectroscopy was employed. The XANES profiles at the Ni *K*-edge of PCN-222-NiCo and PCN-222-Ni are distinctly different from those of Ni foil reference, implying no metal aggregation occurs on the PCN MOF (Figure 1c). Additionally, the Ni spectral features for PCN-222-NiCo remain unchanged upon Co introduction compared with PCN-222-Ni. Both PCN-222-NiCo and PCN-222-Ni exhibit an intense white-line peak and a sharp pre-edge feature centered at 8337 eV arising from the dipole-allowed Ni 1s→4p_z transition, implying the square–planar coordination configuration of Ni in the porphyrin center. One might suspect that there are some subtle differences that could hardly be determined by conventional XANES; therefore, we further performed high-energy-resolution HERFD-XANES measurements at Ni K-edge (Figure S8). Although this technique offers superior energy resolution for probing orbital transitions and geometric symmetry of 3d transition metals compared to conventional XANES, it still fails to resolve any measurable difference between PCN-222-NiCo and PCN-222-Ni, confirming their close similarity in local coordination and electronic state of Ni. The XANES spectrum at the Co *K*-edge for PCN-222-NiCo, also markedly different from the Co foil reference, presents a prominent white-line peak and a distinct pre-edge feature (Figure 1d). The high intensity of the white-line peak suggests a high oxidation state of Co, and the pre-edge peak arises from the partially allowed 1s→3d transition in a non-centrosymmetric coordination environment. The Ni $2p_{3/2}$ x-ray photoelectron spectroscopy (XPS) spectra of PCN-222-NiCo and PCN-222-Ni are almost identical at 854.3 eV, indicating the Ni^{2+} states in both samples and no static structural influence of Co addition to Ni species (Figure S9a). The Co $2p_{3/2}$ spectrum centered at 780.2 eV confirms the dominant Co^{2+} state in PCN-222-NiCo (Figure S9b). The spatially separated Co and Ni sites in the as-prepared state, dictated by steric hindrance, prompts us to carry out operando studies to reveal the actual metal-metal interaction.

15213773, 2026, 45, Downloaded from https://onlinelibrary.wiley.com/doi/10.1002/anie.4551056 by University Of Science, Wiley Online Library on [02/11/2026]. See the Terms and Conditions (https://onlinelibrary.wiley.com/terms-and-conditions) on Wiley Online Library for rules of use; OA articles are governed by the applicable Creative Commons License

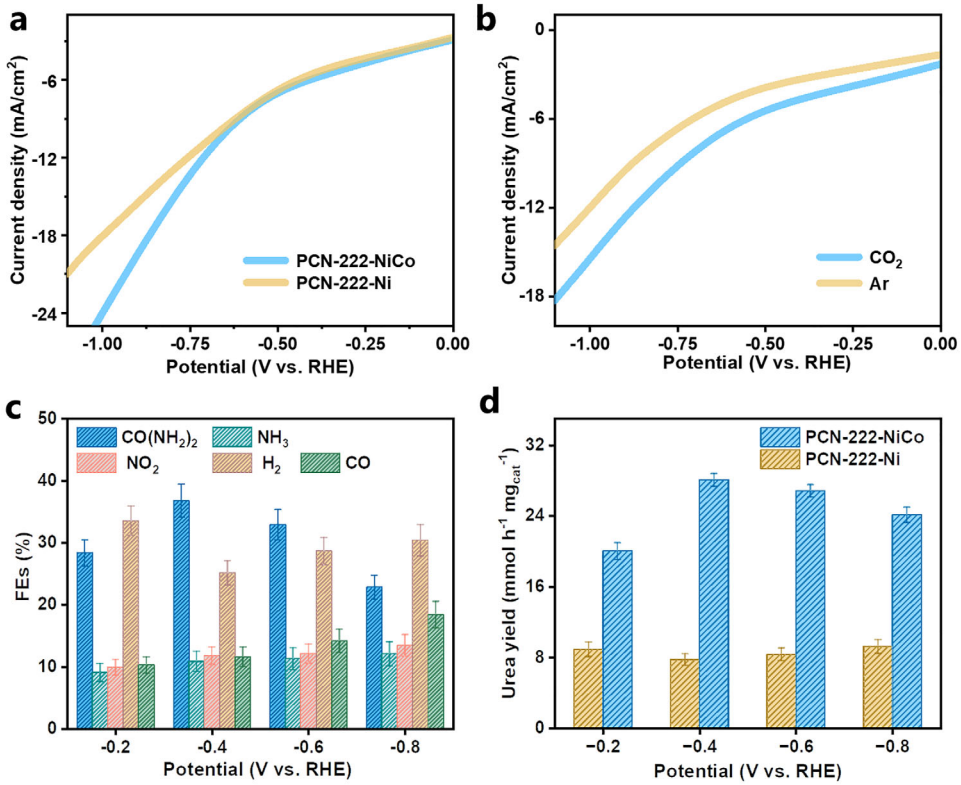


FIGURE 2 | (a) LSV curves of PCN-222-Ni and PCN-222-NiCo catalysts in CO_2-saturated 0.1 M $KHCO_3$ + 0.1 M KNO_3 electrolyte. (b) LSV curves of the PCN-222-NiCo catalyst in 0.1 M KNO_3 electrolyte under Ar and CO_2 atmospheres. (c) Faradaic efficiencies of various products over PCN-222-NiCo catalysts at different applied potentials in CO_2-saturated 0.1 M $KHCO_3$ + 0.1 M KNO_3 electrolyte. (d) Urea yields of PCN-222-NiCo and PCN-222-Ni catalysts at different applied potentials in CO_2-saturated 0.1 M $KHCO_3$ + 0.1 M KNO_3 electrolyte. The error bars represent the standard deviation of three independent measurements ($n = 3$).

To evaluate the catalytic activity of the as-fabricated PCN-222-NiCo catalyst, we systematically investigated its electrocatalytic performance toward the C–N coupling reaction for urea synthesis from CO_2 and NO_3^-, which is environmentally benign, sustainable, and pivotal to closing the carbon-nitrogen cycle. The linear sweep voltammetry (LSV) curves of PCN-222-NiCo and PCN-222-Ni catalysts were tested in a CO_2-saturated 0.1 M $KHCO_3$ + 0.1 M KNO_3 mixed electrolyte, confirming the enhanced electrochemical activity of PCN-222-NiCo catalyst after Co introduction (Figure 2a). The lower charge-transfer resistance of PCN-222-NiCo catalyst implies that the Ni-Co dual-site structure effectively promotes charge transfer, contributing to its superior electrocatalytic performance for C–N coupling reactions (Figure S10). In 0.1 M pure KNO_3 electrolyte, the electrochemical performance of PCN-222-NiCo catalyst is further improved upon CO_2 bubbling compared with Ar atmosphere, which directly verifies the capability for C–N coupling of PCN-222-NiCo (Figure 2b).

The catalytic performance of generated $CO(NH_2)_2$ and byproducts (NH_3 and NO_2^-) on various catalysts were quantified by the diacetylmonoxime method, indophenol blue method and Griess Assay method, respectively (Figures S11–S14). Further evidence that urea originates from nitrate is provided by control experiments, in which no urea was detected in the blank test without nitrate precursors (Figure S15). In addition, the ^{1}H nuclear magnetic resonance (NMR) spectra show good agreement with authentic ^{15}N labeled urea when $^{15}NO_3^-$ is used as the feedstock (Figures S16 and S17). The comparable yields of urea-^{15}N and urea-^{14}N further validate our quantitative analytical approaches and unambiguously demonstrate that urea is produced from dissolved nitrate. It is found that the FE of urea (FE_{urea}) for PCN-222-NiCo reaches a maximum of 36.8% at −0.4 V vs. RHE. The FE of other side products remains low between −0.2 and −0.8 V vs. RHE, with only a modest increase in H_2 production when the applied potential becomes more negative (Figure 2c). In contrast, PCN-222-Ni delivers much lower FE_{urea} across all tested potentials with substantially elevated Faradaic efficiencies for competing byproducts, including H_2, NH_3, and NO_2^- (Figure S18). Moreover, PCN-222-NiCo exhibits significantly higher urea yield than PCN-222-Ni across all tested potentials (Figure 2d). The maximized urea yield of PCN-222-NiCo is achieved at −0.4 V vs. RHE with a value of 28.1 mmol h^{-1} g_{cat}^{-1}, about 3.6 times that of PCN-222-Ni at the same potential. On a Ni basis, the bimetallic PCN-222-NiCo catalyst delivers a turnover frequency (TOF) of 99.9 h^{-1} at −0.4 V vs. RHE, nearly four times that of the monometallic PCN-222-Ni reference with comparable Ni loading under identical conditions (Figure S19). PCN-222-NiCo also maintains stable catalytic activity for over 40 h, demonstrating the structural robustness of the dual-site PCN-222 MOF catalyst. Meanwhile, the 40 h long-term stability test verifies the favorable catalytic stability of the PCN-222-NiCo catalyst, with bimetallic species well retained within the framework (Figure S20 and Table S1). Among non-noble metal dual-site catalytic systems, our PCN-222-NiCo catalyst outperforms most MOF-based

15213773, 2026, 45, Downloaded from https://onlinelibrary.wiley.com/doi/10.1002/anie.4551056 by University Of Science, Wiley Online Library on [02/11/2026]. See the Terms and Conditions (https://onlinelibrary.wiley.com/terms-and-conditions) on Wiley Online Library for rules of use; OA articles are governed by the applicable Creative Commons License

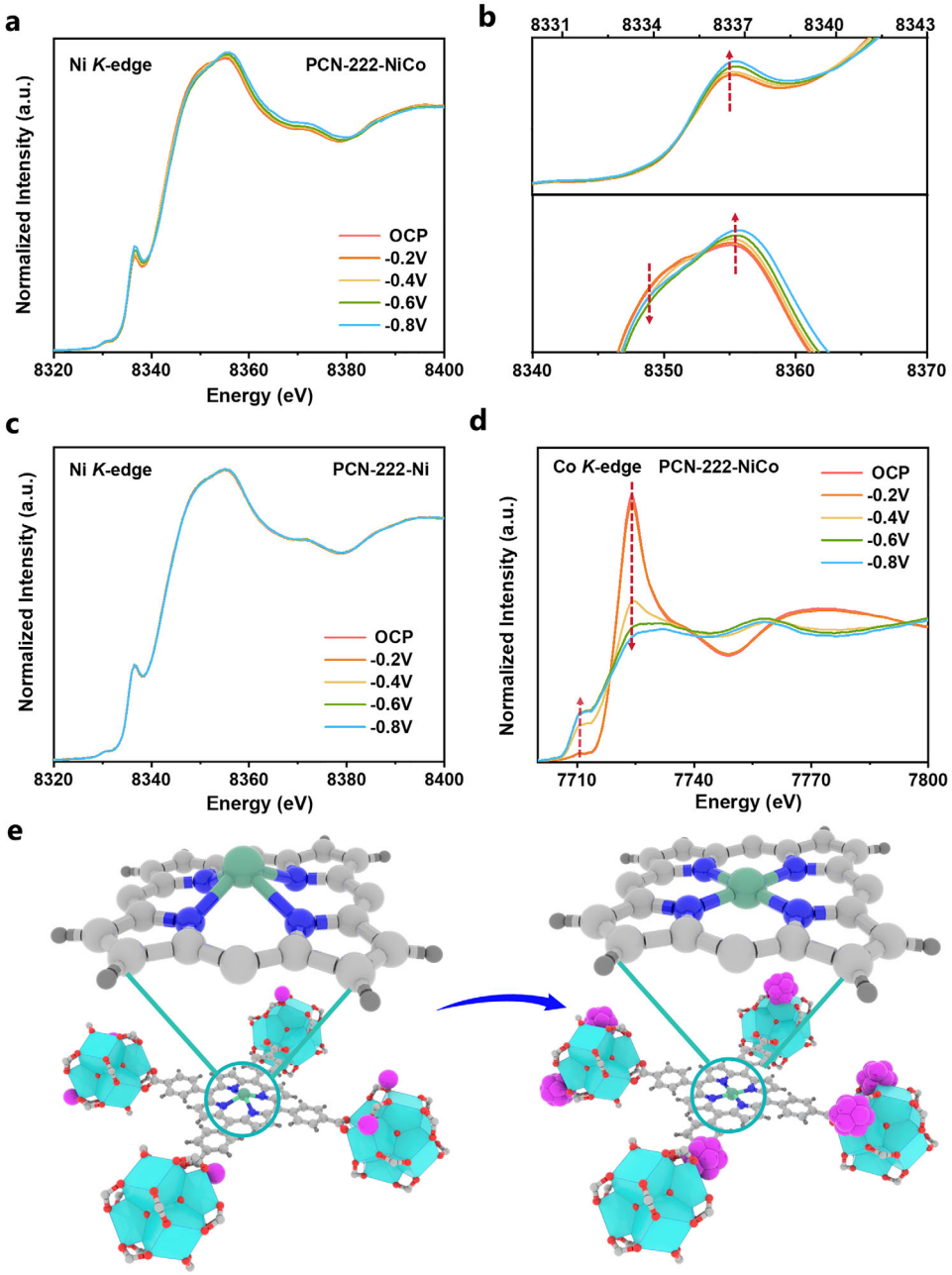


FIGURE 3 | (a and b) In situ XAFS spectra (a) and corresponding magnified views of the pre-edge region (top) and white-line peak region (bottom) (b) at the Ni *K*-edge of PCN-222-NiCo catalyst collected at different potentials during the electrocatalytic C—N coupling reaction. (c) In situ XAFS spectra at the Ni *K*-edge of PCN-222-Ni catalyst. (d) In situ XAFS spectra at the Co *K*-edge of PCN-222-NiCo catalyst. (e) Schematic illustration of the structural evolution of PCN-222-NiCo.

and oxide-based counterparts for electrochemical urea synthesis (Table S2).

To unravel the origin of the superior catalytic activity of the PCN-222-NiCo catalyst, in situ x-ray absorption fine structure (XAFS) measurements were performed to probe the structural evolution of active sites during the electrocatalytic C—N coupling reaction. The in situ Ni *K*-edge XAFS spectra of PCN-222-NiCo were collected at different applied potentials from open circuit potential (OCP) to −0.8 V vs. RHE (Figure 3a). The spectral features show negligible differences between OCP and −0.2 V vs. RHE, while distinct changes appear when the potential is more negative than −0.4 V vs. RHE. Notably, the characteristic peak at 8337 eV, arising from the $1s \rightarrow 4p_z$ transition of Ni in the square–planar structure, is sharply intensified at −0.4 V vs. RHE (Figure 3b), coinciding with the optimal catalytic performance achieved at this potential. Meanwhile, the intensity ratio of the white-line peak features at 8350 and 8356 eV increases with the elevation of negative potential. These spectral changes collectively demonstrate that the planar symmetry of SA Ni sites in PCN-222-NiCo is continuously enhanced with the increase of negative potential. In contrast, no obvious spectral variations are observed for PCN-222-Ni throughout the potential range from OCP to −0.8 V vs. RHE, implying that the presence

15213773, 2026, 45, Downloaded from https://onlinelibrary.wiley.com/doi/10.1002/anie.4551056 by University Of Science, Wiley Online Library on [02/11/2026]. See the Terms and Conditions (https://onlinelibrary.wiley.com/terms-and-conditions) on Wiley Online Library for rules of use; OA articles are governed by the applicable Creative Commons License

TABLE 1 | Structure parameters of PCN-222-NiCo and PCN-222-Ni catalysts under different operating voltage extracted from curve-fittings of in situ EXAFS spectra.

Sample	Edge	Potential	Shell	*N*	*R* (Å)	σ^2 (Å^2)
PCN-222-NiCo	Ni *K*	OCP	Ni–N	4.3 ± 0.2	1.92 ± 0.03	0.005
		−0.4V	Ni–N	4.3 ± 0.2	1.92 ± 0.03	0.004
		−0.8V	Ni–N	4.3 ± 0.2	1.92 ± 0.03	0.003
	Co *K*	OCP	Co–O	6.2 ± 0.5	2.07 ± 0.04	0.007
		−0.4V	Co–Co	5.7 ± 1.1	2.49 ± 0.07	0.005
		−0.8V	Co–Co	7.4 ± 0.6	2.49 ± 0.07	0.005
PCN-222-Ni	Ni *K*	OCP	Ni–N	4.2 ± 0.3	1.92 ± 0.03	0.005
		−0.4V	Ni–N	4.2 ± 0.3	1.92 ± 0.03	0.005
		−0.8V	Ni–N	4.2 ± 0.3	1.92 ± 0.03	0.005

of Co remarkably modulates the potential-responsive behavior of Ni sites in PCN-222-NiCo and further affects its catalytic performance. Besides, as the applied potential increases, the Ni *K*-edge absorption edge of PCN-222-NiCo shifts slightly toward higher energy (Figure S21a). Further fitting analysis of the valence states of Ni atoms reveals a gradual upward trend in Ni valence (Figure S21b).

In situ EXAFS data further corroborates the enhanced planar symmetry of Ni sites in PCN-222-NiCo at more negative potentials. It shows that the $k^2\chi(k)$ oscillatory functions of PCN-222NiCo in the low-*k* region ($k < 6$ Å^{-1}) remain nearly unchanged, whereas amplitudes in the medium and high-*k* region ($k > 6$ Å^{-1}) gradually increase (Figure S22). According to fundamental EXAFS formalism, $k^2\chi(k) \propto N{\cdot}\exp(-2k^2\sigma^2)$, the nearly invariant low-*k* oscillation amplitudes indicate a constant coordination number *N* across potentials. The enhanced high-*k* amplitudes under more negative potentials therefore primarily stem from a reduced Debye–Waller factor σ^2, indicative of improved symmetry around the Ni center. The corresponding Fourier transformed (FT) curves in *R*-space show a prominent first-shell peak at 1.6 Å assigned to Ni–N coordination (Figure S23). This peak intensity rises progressively as the applied potential shifts from OCP to −0.8 V vs. RHE. By contrast, the FT curves of PCN-222-Ni displays no noticeable variations across the entire potential range from OCP to −0.8 V vs. RHE (Figures S24 and S25). Consistently, Wavelet transform (WT) contour plots derived from the Ni *K*-edge EXAFS spectra of PCN-222-NiCo and PCN-222-Ni both exhibit a dominant peak at *R* ~1.6 Å and *k* ~6.2 Å^{-1} across the entire applied potentials. The (*R*, *k*) position of this peak closely matches that of the NiPc reference (Figure S26), confirming that the Ni centers in both catalysts are coordinated by the identical light atoms of nitrogen (N). Quantitative information on the structural evolution could be extracted from curve-fitting analysis of these EXAFS spectra. For the PCN-222-NiCo catalyst (Tables 1 and Figure S27), across OCP, −0.4 V, and −0.8 V vs. RHE, the Ni–N coordination number (*N*) and bond length (*R*) remains nearly constant at 4.3 and 1.92 Å, respectively. Notably, the Debye–Waller factor (σ^2) decreases progressively from 0.005 Å^2 at OCP, to 0.004 Å^2 at −0.4 V vs. RHE, and further to 0.003 Å^2 at −0.8 V vs. RHE. The gradual decline in σ^2 indicates reduced structural disorder, further corroborating the potential-induced enhancement in the planar symmetry of Ni–N_4 sites as revealed by the in situ XANES spectra. For the PCN-222-Ni catalyst, the Ni–N *N* of 4.2, *R* of 1.92 Å, and σ^2 of 0.005 Å^2 all remain unchanged throughout the potential range. All these results demonstrate that the existence of Co species modulates the planar coordination geometry of Ni sites.

Complementary to Ni *K*-edge characterization, in situ Co *K*-edge XAFS spectra were also collected to track the structural evolution of Co species in PCN-222-NiCo. From OCP to −0.2 V vs. RHE, the Co *K*-edge XANES spectra show slightly reduced white-line intensity while retaining the feature of dispersed Co sites (Figure 3c). At −0.4 V vs. RHE, the pre-edge peak at 7711 eV is significantly intensified and the white-line peak at 7732 eV is sharply attenuated, suggesting the reduction of Co^{2+} to metallic Co. The continuous formation of metallic Co species is further verified by the EXAFS $k^2\chi(k)$ spectra, which display intensified high-*k* oscillation amplitudes at −0.4 and −0.8 V vs. RHE, closely resembling the profile of Co foil (Figure S28). In comparison with the FT curve in R space at OCP showing a prominent Co–O peak at 1.6 Å, a new Co–Co coordination peak at 2.1 Å appears at −0.4 V and intensifies further at −0.8 V vs. RHE, indicating the progressive transformation of SA Co sites into metallic NPs (Figure S29), which is confirmed by the WT analysis (Figure S30). Quantitative EXAFS fitting results (Table 1 and Figure S31) demonstrate that at OCP, Co sites exhibit Co–O coordination with a coordination number of 6.2, a bond length of 2.07 Å, and a σ^2 value of 0.007 Å^2. At −0.4 V vs. RHE, the coordination environment fully converts to Co—Co bonding (N = 5.7, R = 2.49 Å, σ^2 = 0.005 Å^2). Further increasing the negative bias only increases the Co–Co coordination number to 7.4 with unchanged *R* and σ^2, indicating saturated Co NP growth. Post-reaction TEM images validate such structural evolutions. No metallic precipitation occurs on PCN-222-Ni, confirming the high stability of SA Ni sites during the reaction (Figure S32). In contrast, PCN-222-NiCo exhibits homogeneous dispersion with an average diameter of 1.6 nm after reaction (Figure S33), which originates exclusively from Co reconstruction rather than Ni precipitation or NiCo alloy formation during the potential-driven transformation. The close proximity is further observed through the HAADF-STEM image, clearly revealing that Ni SAs are distributed in a planetary pattern surrounding the Co NP (Figure S34).

15213773, 2026, 45, Downloaded from https://onlinelibrary.wiley.com/doi/10.1002/anie.4551056 by University Of Science, Wiley Online Library on [02/11/2026]. See the Terms and Conditions (https://onlinelibrary.wiley.com/terms-and-conditions) on Wiley Online Library for rules of use; OA articles are governed by the applicable Creative Commons License

To validate the in situ evolved Co NPs driving the enhanced Ni—N_4 symmetry and C—N coupling performance, we prepared a physical mixture of PCN-222-Ni and static Co NPs as a control. For better comparison, the NU-1000 with a crystal structure similar to PCN-222 was employed to load Co sites (Figures S35 and S36), which could be exclusively immobilized on Zr–oxo clusters by replacing porphyrin tetracarboxylic acid with pyrenetetracarboxylic acid. TEM images show the Co NPs loaded on NU-1000 (Figure S37). Strikingly, when NU-1000-Co was physically mixed with PCN-222-Ni, preformed Co NPs suppress the activity of PCN-222-Ni, delivering a urea yield below 7.9 mmol h^{-1} $g_{cat}{}^{-1}$ at all potentials and FE_{urea} below 16.7%, in sharp contrast to the superior activity of the PCN-222-NiCo catalyst. Therefore, only in situ evolved Co NPs could promote the activity of Ni sites (Figure S38). Besides, a monometallic PCN-222-Co control sample shows negligible urea activity, verifying that isolated Co sites cannot drive efficient C—N coupling (Figures S39 and S40). TEM characterization of the reduced PCN-222-NiCo in H_2 at 300°C for 2 h reveals that high-temperature reduction retains the intact structure without metal precipitation, which simultaneously verifies the superior thermal stability of the catalyst and confirms that Co NPs form only under in situ electrochemical conditions (Figures S41 and S42). Collectively, all these results reveal that the dynamic reduction of SA Co sites into metallic NP species acts as the critical trigger for the progressive symmetry enhancement of Ni–N_4 SA sites. The dynamic structural transformation of Ni–Co dual sites is schematically illustrated (Figure 3e). In the initial state, the PCN-222-NiCo catalyst possesses spatially separated Ni and Co SA sites with a relatively long distance between the two metal sites. During the electrocatalytic C–N coupling reaction, the Co SA sites are gradually in situ reduced and agglomerated to form Co NPs, which induces the continuous enhancement of the planar symmetry of the adjacent Ni–N_4 SA sites and enables the creation of a tightly coupled dual-site structure with proximal Co NPs and SA Ni sites at porphyrin centers.

To unravel the intrinsic catalytic mechanism for PCN-222-NiCo catalyst, the in situ Raman spectroscopy, synchrotron radiation Fourier-transform infrared spectroscopy (SR-FTIR), and differential electrochemical mass spectrometry (DEMS) were used to track the evolution of reaction intermediates and key coupling species. The in situ Raman spectra reveal that both PCN-222-NiCo and PCN-222-Ni show characteristic NO_2^- vibrations at 836/838 cm^{-1}, verifying efficient NO_3^- activation on the Ni–N_4 sites (Figure 4a,b). Notably, a vibration peak assigned to adsorbed *NO appears at 2111 cm^{-1} for PCN-222-NiCo, which is hardly visible for PCN-222-Ni (Figure 4a), demonstrating the promoted NO_3^- conversion toward *NO intermediates on PCN-222-NiCo. Furthermore, PCN-222-NiCo exhibits three peaks assigned to the restricted stretching vibration of *CO (2066 and 2023 cm^{-1}) and *COOH (780 cm^{-1}) species at −0.4 V vs. RHE, while these CO_2-derived intermediates cannot be detected on PCN-222-Ni (Figure 4b), confirming selective CO_2 adsorption and activation on the in situ-generated Co NPs. More importantly, a distinct peak at 2241 cm^{-1} appears and intensifies with increasing negative potential (Figure 4a). This signal is assigned to the N—C—O stretching mode of urea intermediates, evidencing efficient C—N coupling induced by the Ni–Co dual-site synergistic effect.

The in situ SR-FTIR spectra of PCN-222-NiCo catalyst display a series of characteristic product/intermediate peaks of *$CONH_2$ (1780 cm^{-1}), *NH_2 (1583 cm^{-1}), C—N (1434 cm^{-1}), *CO (1378 cm^{-1}) and NO_2^- (1342/1350 cm^{-1}) associated with NO_3^- reduction reaction (NO_3RR), CO_2 reduction reaction (CO_2RR), and C–N coupling (Figure 4c). These peaks emerge sequentially as the applied potential shifts negatively. In sharp contrast, the PCN-222-Ni only exhibits vibration peaks ascribed to NO_2^-, which is fully consistent with previous in situ Raman results and further validates that Ni sites serve as the active centers for NO_3RR (Figure 4d). The distinct peak of *CO (1378 cm^{-1}) observed on PCN-222-NiCo verifies that Co sites act as the active sites for CO_2 activation and reduction (Figure 4c). Besides, the emergence of vibration peak of *NH_2 at 1583 cm^{-1} implies that the enhanced-symmetry Ni—N_4 sites induced by evolved Co NPs further promote the conversion of key *NH_2 intermediate from *NO and enable subsequent C—N coupling. The stretching vibration peak of *$CONH_2$ at 1780 cm^{-1} gradually intensifies with increasing negative potential. This peak represents the first direct spectroscopic signature of C—N coupling initiation, and unambiguously demonstrates that the Ni—Co dual sites in PCN-222-NiCo synergistically trigger the efficient coupling of NO_3^- and CO_2. The observed red shift of all key N-containing vibrational bands in the ^{15}N isotopic in situ FTIR spectra confirms the accurate assignment of the key reaction intermediates (Figure S43). In addition, in situ DEMS analysis suggests that the signal intensity at m/z = 44 identified as the critical *$CONH_2$ intermediate for PCN-222-NiCo is much higher than that of PCN-222-Ni, providing direct mass-spectrometric evidence for efficient C—N bond formation (Figure S44).

To uncover the correlation between Ni—N_4 site symmetry and nitrate-reduction performance, we performed DFT calculations. Model structures were constructed with different tilt angles θ (ranging from 10° to 0°) between the Ni—N_4 center and the carbon-based porphyrin coordination plane. The configuration with $\theta = 10°$ mimics the low symmetry Ni–N_4 (LS Ni—N_4, $\theta = 10°$), whereas the configuration with $\theta = 0°$ mimics the high symmetry Ni—N_4 (HS Ni—N_4, $\theta = 0°$). We calculated the NO_3^- adsorption energy on these Ni–N_4 configurations (Figures 5a and S45). The results indicate that the adsorption energy of NO_3^- on Ni—N_4 configuration drops with continuous symmetry-enhancement. Specifically, the low-symmetry Ni—N_4 (LS Ni—N_4, θ = 10°) shows a positive NO_3^- adsorption energy of 0.73 eV, implying thermodynamically unfavorable adsorption. With increasing planar symmetry (θ decreases to 0°), the adsorption energy turns gradually negative, reaching −0.75 eV for the high-symmetry Ni—N_4 (HS Ni—N_4, $\theta = 0°$) structure, proving that the enhanced planar symmetry of Ni—N_4 effectively strengthens NO_3^- adsorption which serves as a prerequisite for efficient subsequent reduction. The partial density of states (PDOS) of Ni 3d orbitals further reveals the electronic origin of the symmetry-dependent adsorption behavior (Figure 5b). After NO_3^- adsorption, the d-band center of the HS Ni—N_4 site (−1.77 eV) is notably lower than that of the LS Ni–N_4 site (−1.53 eV). The pronounced d-band downshift on the HS Ni—N_4 site reflects stronger orbital hybridization between Ni 3d orbitals and the orbitals of NO_3^-. The enhanced backdonation from Ni 3d to the antibonding orbitals of NO_3^- weakens the N—O bonds and thus activates NO_3^-.

The relative energy diagrams for the NO_3RR pathway on Ni sites are analyzed based on HS Ni—N_4 and LS Ni—N_4

15213773, 2026, 45, Downloaded from https://onlinelibrary.wiley.com/doi/10.1002/anie.4551056 by University Of Science, Wiley Online Library on [02/11/2026]. See the Terms and Conditions (https://onlinelibrary.wiley.com/terms-and-conditions) on Wiley Online Library for rules of use; OA articles are governed by the applicable Creative Commons License

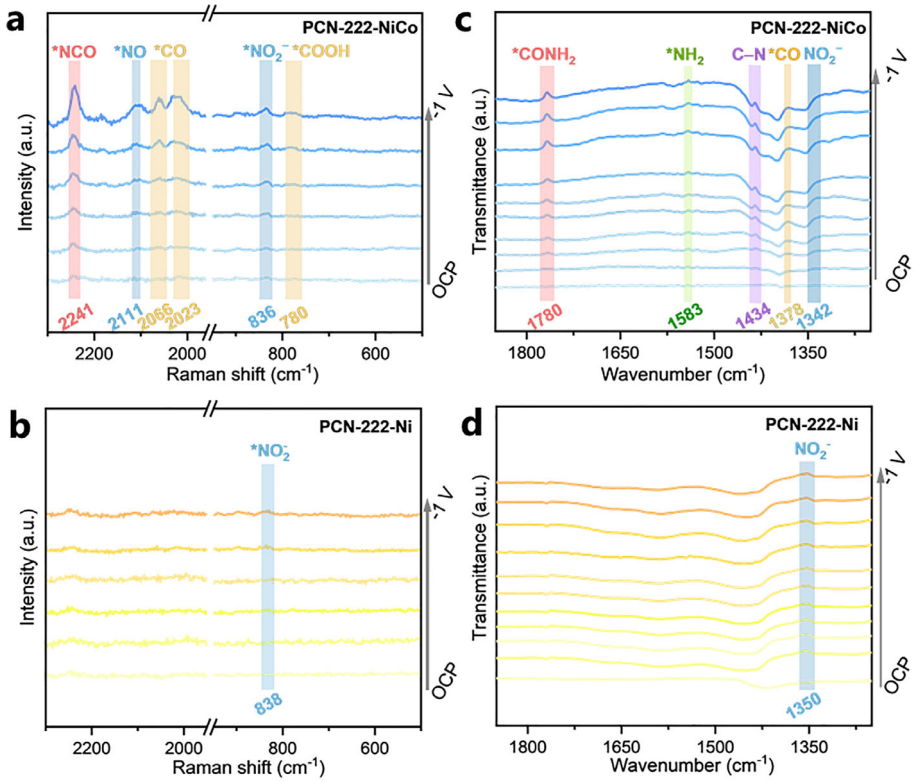


FIGURE 4 | (a and b) In situ Raman spectra of PCN-222-NiCo (a) and PCN-222-Ni (b) at different potentials under electrocatalytic C–N coupling. (c and d) In situ SR-FTIR spectra of reaction intermediates on PCN-222-NiCo (c) and PCN-222-Ni (d) recorded at different potentials under electrocatalytic C–N coupling in CO_2-saturated 0.1 M $KHCO_3$ + 0.1 M KNO_3 electrolyte.

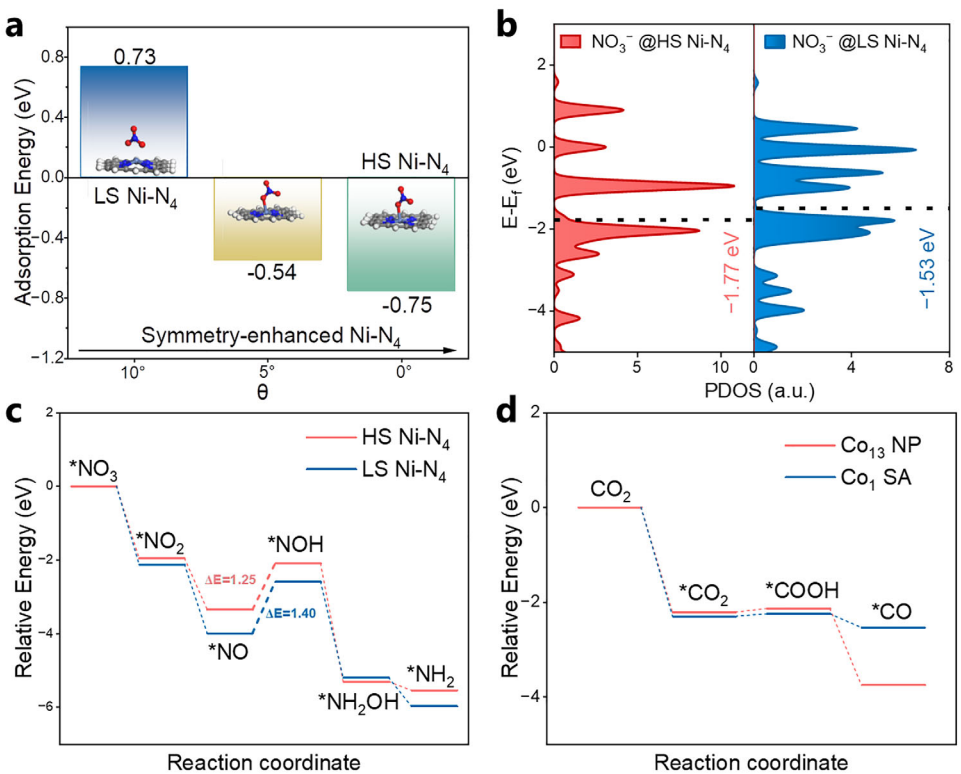


FIGURE 5 | (a) DFT calculation of adsorption energies of NO_3^- on Ni—N_4 configurations with continuously enhanced in-plane symmetry, where the tilt angle θ between the Ni active center and the coordination plane decreases from 10° to 0°. (b) PDOS of NO_3^--adsorbed HS Ni—N_4 site and NO_3^--adsorbed LS Ni—N_4 site. Atom color-coding: blue for N; green gray for Ni; red for O; gray for C; white for H. (c and d) The relative energy for NO_3RR on HS Ni—N_4 and LS Ni—N_4 sites (c) and CO_2RR on Co_{13} NP and Co_1 SA sites (d) for C—N coupling.

15213773, 2026, 45, Downloaded from https://onlinelibrary.wiley.com/doi/10.1002/anie.4551056 by University Of Science, Wiley Online Library on [02/11/2026]. See the Terms and Conditions (https://onlinelibrary.wiley.com/terms-and-conditions) on Wiley Online Library for rules of use; OA articles are governed by the applicable Creative Commons License

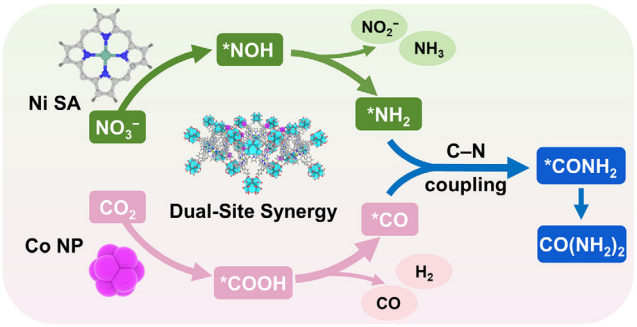


FIGURE 6 | Proposed dual-site synergistic reaction mechanism pathway for electrocatalytic C—N coupling to urea over PCN-222-NiCo catalyst.

model sites (Figures 5c and S46–S48). The overall reaction proceeds through consecutive proton-electron transfer steps: $*NO_3 \rightarrow *NO_2 \rightarrow *NO \rightarrow *NOH \rightarrow *NH_2OH \rightarrow *NH_2$. The results reveal that the conversion from *NO to *NOH is identified as the rate-determining step (RDS) of the entire NO_3RR process for both configurations. Remarkably, the RDS energy barrier on the LS Ni—N_4 site is calculated to be 1.40 eV, while this value is significantly reduced to 1.25 eV on the HS Ni—N_4 site. This barrier reduction directly proves that the enhancement of planar symmetry kinetically accelerates the rate-limiting step of nitrate reduction for promoting enrichment of nitrogen-containing intermediates.

For the CO_2RR process on Co sites, we compared the reaction energetics over Co_{13} NP and Co_1 SA model sites, corresponding to the in situ reconstructed state and the initial pristine state, respectively (Figures 5d, S49, and S50). The reaction follows the pathway of $CO_2 \rightarrow *CO_2 \rightarrow *COOH \rightarrow *CO$. The two configurations show similar energy barriers for the *COOH formation step, but exhibit significant differences in the final formation of *CO, with energy difference from *COOH→*CO of −0.29 eV on Co_1 SA and −1.61 eV on Co_{13} NP, indicating that *CO formation on in situ evolved Co NP is thermodynamically more favorable and spontaneous. This results in a sufficiently high surface concentration of *CO species around the active sites, creating favorable conditions for the subsequent C—N coupling reaction.

Based on the above analysis, the synergy of the symmetry-optimized Ni—N_4 sites with the adjacent in situ-formed Co NPs is the cornerstone for efficient C—N coupling (Figure 6). The reaction pathway and the origin of superior activity for electrocatalytic C—N coupling over PCN-222-NiCo are elucidated. The potential-driven in situ reduction of Co SAs to metallic NPs, coupled with the concurrent enhancement in planar symmetry of the proximal Ni—N_4 sites, creates a unique and tightly coupled dual-site architecture. In this synergistic system, the symmetry-optimized Ni—N_4 sites provide an electronically favorable configuration for the selective adsorption and activation of NO_3^-, efficiently reducing the *NO-to-*NOH barrier and channeling it toward the *NH_2 intermediate. Simultaneously, the in situ generated Co NPs facilitate the formation of *CO intermediate from *COOH for activation of CO_2. The spatial proximity between these two distinct sites ensures effective interaction. Critically, the electronic fine-tuning of the Ni sites via symmetry enhancement imparts a higher nucleophilicity to the generated *NH_2 intermediate, enabling its efficient coupling with the *CO intermediate on adjacent Co sites to form the pivotal *$CONH_2$ species. This dual-site synergistic mechanism, underpinned by the structural and electronic optimization of the Ni center, achieves spatially separated and energetically favorable activation of nitrate and carbon dioxide, stabilizes the rate-determining *$CONH_2$ intermediate, and mitigates competitive side reactions. As a result, PCN-222-NiCo delivers outstanding electrocatalytic performance for C—N coupling toward urea synthesis.

3 | Conclusions

In summary, PCN-222-NiCo with SA Ni anchored on porphyrin ligands and SA Co immobilized on Zr–oxo clusters is rationally synthesized. The catalyst delivers outstanding performance toward electrocatalytic urea synthesis, affording a peak urea FE of 36.8% and a yield of 28.1 mmol $h^{-1}g_{cat}^{-1}$ at −0.4 V vs. RHE, which is around 3.6-fold higher than the single-site Ni SA counterpart. In situ characterizations and DFT calculations confirm that Co SAs dynamically evolve into Co NP, which is responsible for facilitating the *COOH-to-*CO conversion during electrolysis, and simultaneously enhances the planar symmetry of the Ni—N_4 sites to an optimized Ni 3d electronic configuration that lowers the *NO-to-*NOH RDS barrier. The proximal symmetry-enhanced SA Ni sites and in-situ evolved Co NPs within MOFs minimize the diffusion distance of *NH_2 and *CO intermediates and accelerates the production of the key *$CONH_2$ intermediate via favorable C—N coupling. This study offers an effective strategy to construct neighboring synergistic dual sites in MOFs for high-efficiency electrocatalytic coupling reactions.

Author Contributions

Ruichao Xu: conceptualization, methodology, investigation, visualization, writing – original draft, writing – review and editing, formal analysis, supervision. **Zhenyang Dai:** methodology, software, data curation, investigation, validation. **Weizhi Gu:** investigation, validation, formal analysis, conceptualization. **Weiqi Lu:** conceptualization, validation, software. **Fengtang Zhao:** methodology, investigation. **Lingshan Qu:** investigation, data curation. **Jinglin Yuan:** conceptualization, methodology. **Yajuan Feng:** software, formal analysis, data curation, visualization. **Long Jiao:** writing – review and editing, conceptualization, methodology, funding acquisition. **Hai-Long Jiang:** conceptualization, project administration, resources. **Zhihu Sun:** writing – original draft, writing – review and editing, conceptualization, methodology, project administration, resources, funding acquisition, visualization.

Acknowledgments

The authors thank National Key Research and Development Program of China (No. 2021YFA1500403), the National Natural Science Foundation of China (Grant Numbers. 12375329, 12275271, 22375193 and 22575235) for financial support. They also greatly appreciate the synchrotron radiation beamline BL01B of National Synchrotron Radiation Laboratory (NSRL) and BL20U of Shanghai Synchrotron Radiation Facility (SSRF).

Conflicts of Interest

The authors declare no conflicts of interest.

15213773, 2026, 45, Downloaded from https://onlinelibrary.wiley.com/doi/10.1002/anie.4551056 by University Of Science, Wiley Online Library on [02/11/2026]. See the Terms and Conditions (https://onlinelibrary.wiley.com/terms-and-conditions) on Wiley Online Library for rules of use; OA articles are governed by the applicable Creative Commons License

Data Availability Statement

The data that support the findings of this study are available from the corresponding author upon reasonable request.

References

1. Q. Qian, Q. Liu, M. Wang, et al., "Dual-Site Cooperation for Synergistic Optimization of the Band Structure and Spin State to Facilitate C–N Coupling Reaction," *Proceedings of the National Academy of Sciences* 122 (2025): e2508077122, https://doi.org/10.1073/pnas.2508077122.

2. M. Xu, M. Wang, H. Wang, P. Yuan, Q. Han, and G. Zheng, "Electrocatalytic and Photocatalytic C–N Coupling From Small Molecules," *Advanced Materials* 38 (2026): 2507144, https://doi.org/10.1002/adma.202507144, n/a.

3. Y. Zuo, D. Yu, X. Zhang, and X. Wang, "Electrocatalytic C—N Coupling in Aqueous Solutions for High-Value Product Synthesis," *Angewandte Chemie International Edition* 65 (2026): e18370, https://doi.org/10.1002/anie.202518370.

4. Y. Yu, J. Li, Z. Yue, et al., "Advances in Multiple Active Site Catalysts for Urea Synthesis via Electrocatalytic C–N Coupling," *Transactions of Tianjin University* 31 (2025): 478–497, https://doi.org/10.1007/s12209-025-00444-2.

5. Q. Hu, W. Zhou, S. Qi, et al., "Pulsed Co-Electrolysis of Carbon Dioxide and Nitrate for Sustainable Urea Synthesis," *Nature Sustainability* 7 (2024): 442–451, https://doi.org/10.1038/s41893-024-01302-0.

6. Y. Zhou, G. Xing, C. Sun, et al., "Electrosynthesis of Urea From Carbon Dioxide and Waste Nitrates: History, Recent Progress, and Future Prospects," *Advanced Functional Materials* 36 (2025): e15635, https://doi.org/10.1002/adfm.202515635.

7. Y. Zhou, C. Feng, C. Sun, et al., "Urea Electrosynthesis From Gaseous Nitrogen Oxides and Carbon Dioxide: A Review," *Materials Today Catalysis* 11 (2025): 100128, https://doi.org/10.1016/j.mtcata.2025.100128.

8. M. Xu, M. Wang, H. Wang, et al., "Electrocatalytic and Photocatalytic C Horizontal Line N Coupling From Small Molecules," *Advanced Materials* 38 (2025): e2507144, https://doi.org/10.1002/adma.202507144.

9. C. Chen, N. He, and S. Wang, "Electrocatalytic C–N Coupling for Urea Synthesis," *Small Science* 1 (2021): 2100070, https://doi.org/10.1002/smsc.202100070.

10. L. Lv, H. Tan, Y. Kong, et al., "Breaking the Scaling Relationship in C—N Coupling via the Doping Effects for Efficient Urea Electrosynthesis," *Angewandte Chemie International Edition* 63 (2024): e202401943, https://doi.org/10.1002/anie.202401943.

11. X. Zhang, X. Zhu, S. Bo, et al., "Identifying and Tailoring C–N Coupling Site for Efficient Urea Synthesis Over Diatomic Fe–Ni Catalyst," *Nature Communications* 13 (2022): 5337, https://doi.org/10.1038/s41467-022-33066-6.

12. Y. Zhao, Y. Ding, W. Li, et al., "Efficient Urea Electrosynthesis From Carbon Dioxide and Nitrate via Alternating Cu–W Bimetallic C–N Coupling Sites," *Nature Communications* 14 (2023): 4491, https://doi.org/10.1038/s41467-023-40273-2.

13. X.-Y. Dong, Y.-J. Jin, H. Chen, B. Li, S.-Q. Zang, and J. Cai, "Atomic-Level Dynamic Spacing Engineering in COF-Based Electrocatalysts for Urea Synthesis in Ultra-Low and Wide Potential Ranges," *Science Bulletin* 71 (2026): 1380–1386, https://doi.org/10.1016/j.scib.2026.01.060.

14. C. S. Gerke, M. Klenk, P. Zapol, and V. S. Thoi, "Pulsed-Potential Electrolysis Enhances Electrochemical C–N Coupling by Reorienting Interfacial Ions," *ACS Catalysis* 13 (2023): 14540–14547, https://doi.org/10.1021/acscatal.3c03027.

15. C. Lv, L. Zhong, H. Liu, et al., "Selective Electrocatalytic Synthesis of Urea With Nitrate and Carbon Dioxide," *Nature Sustainability* 4 (2021): 868–876, https://doi.org/10.1038/s41893-021-00741-3.

16. Y. Zhong, H. Xiong, J. Low, R. Long, and Y. Xiong, "Recent Progress in Electrochemical C–N Coupling Reactions," *eScience* 3 (2023): 100086, https://doi.org/10.1016/j.esci.2022.11.002.

17. W. Bai, H. Zeng, F. Chen, et al., "Emerging Atomistic Modeling Catalysts for C—N Electrocatalysis," *Advanced Materials* 38 (2026): e10907, https://doi.org/10.1002/adma.202510907.

18. X. Wu, Y. Chen, B. Tang, et al., "CeO_x-Integrated Dual Site Enhanced Urea Electrosynthesis From Nitrate and Carbon Dioxide," *Nature Communications* 16 (2025): 8785, https://doi.org/10.1038/s41467-025-63839-8.

19. Y. Wan, M. Zheng, W. Yan, J. Zhang, and R. Lv, "Fundamentals and Rational Design of Heterogeneous C-N Coupling Electrocatalysts for Urea Synthesis at Ambient Conditions," *Advanced Energy Materials* 14 (2024): 2303588, https://doi.org/10.1002/aenm.202303588.

20. L. Liu and A. Corma, "Bimetallic Sites for Catalysis: From Binuclear Metal Sites to Bimetallic Nanoclusters and Nanoparticles," *Chemical Reviews* 123 (2023): 4855–4933, https://doi.org/10.1021/acs.chemrev.2c00733.

21. Y. Li, Y. Li, H. Sun, et al., "Current Status and Perspectives of Dual-Atom Catalysts Towards Sustainable Energy Utilization," *Nano-Micro Letters* 16 (2024): 139, https://doi.org/10.1007/s40820-024-01347-y.

22. P.-Y. Shi, Y. Yan, S.-Y. Yang, J.-J. Hao, M. Wang, and T.-B. Lu, "Dual-Metal Synergistic Catalysis for Promoting Electrocatalytic CO_2 Reduction," *Chemical Science* 16 (2025): 11711–11739, https://doi.org/10.1039/D5SC03193A.

23. N. Sun, S. S. A. Shah, Z. Lin, Y.-Z. Zheng, L. Jiao, and H.-L. Jiang, "MOF-Based Electrocatalysts: An Overview From the Perspective of Structural Design," *Chemical Reviews* 125 (2025): 2703–2792, https://doi.org/10.1021/acs.chemrev.4c00664.

24. C. Zhang, Z. Lin, L. Jiao, and H.-L. Jiang, "Metal–Organic Frameworks for Electrocatalytic CO_2 Reduction: From Catalytic Site Design to Microenvironment Modulation," *Angewandte Chemie International Edition* 63 (2024): e202414506, https://doi.org/10.1002/anie.202414506.

25. Y. Peng, S. Sanati, A. Morsali, and H. García, "Metal–Organic Frameworks as Electrocatalysts," *Angewandte Chemie International Edition* 62 (2023): e202214707, https://doi.org/10.1002/anie.202214707.

26. J. Zhao, X. Wang, X. Yan, M. Liu, N. Li, and X.-H. Bu, "Reconstruction of Metal-Organic Frameworks for Enhanced Electrocatalytic Performance," *Advanced Materials* 38 (2026): e23668, https://doi.org/10.1002/adma.202523668.

27. I. Senkovska, Y. Luo, R. Zhao, et al., "Electroactive Metal–Organic Frameworks for Electrocatalysis," *Advanced Functional Materials* 36 (2026): e12141, https://doi.org/10.1002/adfm.202512141.

28. T. Chen, Z. Tan, H. Xu, et al., "Electrochemical Reconstruction of Defect Engineered MOFs: A Dynamic Frontier in Electrochemistry," *Advanced Functional Materials* 36 (2026): e17710, https://doi.org/10.1002/adfm.202517710.

29. B. Li, H.-M. Wen, Y. Cui, W. Zhou, G. Qian, and B. Chen, "Emerging Multifunctional Metal–Organic Framework Materials," *Advanced Materials* 28 (2016): 8819–8860, https://doi.org/10.1002/adma.201601133.

30. F. Zheng, T. Lin, K. Wang, Y. Wang, and G. Li, "Recent Advances in Bimetallic Metal-Organic Frameworks and Their Derivatives for Thermal Catalysis," *Nano Research* 16 (2023): 12919–12935, https://doi.org/10.1007/s12274-023-5935-0.

31. H. Wang, L. Yang, Y. Yang, and L. Jia, "Multifunctional Bimetallic MOF Engineering: Innovative Synthesis and Versatile Applications in Adsorption, Catalysis, Sensing, and Energy," *Coordination Chemistry Reviews* 547 (2026): 217114, https://doi.org/10.1016/j.ccr.2025.217114.

32. E. Tiburcio, Y. Zheng, C. Bilanin, et al., "MOF-Triggered Synthesis of Subnanometer $Ag^0{}_2$ Clusters and Fe^{3+} Single Atoms: Heterogenization Led to Efficient and Synergetic One-Pot Catalytic Reactions," *Journal of the American Chemical Society* 145 (2023): 10342–10354, https://doi.org/10.1021/jacs.3c02155.

33. J. Ballesteros-Soberanas, N. Martín, M. Bacic, et al., "A MOF-Supported Pd_1–Au_1 Dimer Catalyses the Semihydrogenation Reaction

15213773, 2026, 45, Downloaded from https://onlinelibrary.wiley.com/doi/10.1002/anie.4551056 by University Of Science, Wiley Online Library on [02/11/2026]. See the Terms and Conditions (https://onlinelibrary.wiley.com/terms-and-conditions) on Wiley Online Library for rules of use; OA articles are governed by the applicable Creative Commons License

of Acetylene in Ethylene With a Nearly Barrierless Activation Energy," *Nature Catalysis* 7 (2024): 452–463, https://doi.org/10.1038/s41929-024-01130-7.

34. P. Feng, S. Wang, Z. Dai, et al., "Stable $Cu^{\delta+}$ Sites Derived From Analogous Rectifying Interface in AgCu Biphasic Aerogels for Efficient Urea Electrosynthesis at Low Potential," *Nature Communications* 17 (2026): 59, https://doi.org/10.1038/s41467-025-65857-y.

35. Y. Wang, S. Xia, J. Zhang, et al., "Regulating Active Hydrogen Supply Over Cu Clusters-Interspersed MoS_2/MoO_2 Nanosheets for Efficient Urea Electrosynthesis," *Advanced Functional Materials* 36 (2026): e19152, https://doi.org/10.1002/adfm.202519152.

36. Z. Feng, L.-H. Zhang, Y. Guo, J. Guo, F. Li, and F. Yu, "Charge Polarization Boosting Electrochemical Urea Synthesis by Co-Reduction of CO_2 and Nitrite in Dilute Concentrations With a Unity Carbon Selectivity," *Angewandte Chemie International Edition* 64 (2025): e202500262, https://doi.org/10.1002/anie.202500262.

37. J. Jiang, G. Wu, M. Sun, et al., "Cu–Mo Dual Sites in Cu-Doped $MoSe_2$ for Enhanced Electrosynthesis of Urea," *ACS Nano* 18 (2024): 13745–13754, https://doi.org/10.1021/acsnano.4c01821.

38. C. Xia, F.-M. Li, C. He, S. Zaman, W. Guo, and B. Y. Xia, "Structural Reconstruction of Electrocatalysts," *Fundamental Research* 5 (2025): 2537–2552, https://doi.org/10.1016/j.fmre.2024.04.017.

39. H. Chen, L. Wang, M. Na, and X. Zou, "Reconstruction Chemistry of Electrocatalysts Under Working Conditions," *Chemical Science* 16 (2025): 20662–20676, https://doi.org/10.1039/D5SC06605.

40. Y. Zhao, N. Dongfang, R. Erni, M. Iannuzzi, and G. R. Patzke, "Dynamics and Control of Dual Active Sites in Co-Substituted Ni Coordination Polymers for Enhanced Oxygen Evolution Catalysis," *Journal of the American Chemical Society* 148 (2026): 3976–3986, https://doi.org/10.1021/jacs.5c12205.

41. S. Tian, R. Wu, H. Liu, et al., "Realizing Unconventional Tandem Nitrate Reduction for Efficient Ammonia Electrosynthesis Enabled by Co, Fe Dual-Site Conjugated Metal Organic Frameworks," *Angewandte Chemie International Edition* 64 (2025): e202510665, https://doi.org/10.1002/anie.202510665.

42. Q. Li, C. Jia, Q. Wang, et al., "Rational Design of Conductive MOF-Based Diatomic Electrocatalysts for Selective Ammonia Synthesis," *Journal of the American Chemical Society* 147 (2025): 39430–39439, https://doi.org/10.1021/jacs.5c11655.

43. X. Yao, W. Li, D. Cui, et al., "Dual-Metal Sites in MOF Synergistic Boosting NH_3 Production Under Low-Nitrate Concentration," *Nano Research* 18 (2025): 94907592, https://doi.org/10.26599/NR.2025.94907592.

44. D. Feng, Z.-Y. Gu, J.-R. Li, H.-L. Jiang, Z. Wei, and H.-C. Zhou, "Zirconium-Metalloporphyrin PCN-222: Mesoporous Metal–Organic Frameworks With Ultrahigh Stability as Biomimetic Catalysts," *Angewandte Chemie International Edition* 51 (2012): 10307–10310, https://doi.org/10.1002/anie.201204475.

45. G. Yang, W. Shi, Y. Qian, X. Zheng, Z. Meng, and H.-L. Jiang, "Turning on Asymmetric Catalysis of Achiral Metal-Organic Frameworks by Imparting Chiral Microenvironment," *Angewandte Chemie International Edition* 62 (2023): e202308089, https://doi.org/10.1002/anie.202308089.

46. Y. Jiang, Z. Chen, T. Peng, et al., "Single-Atom Fe Catalysts With Improved Metal Loading for Efficient Ammonia Synthesis Under Mild Conditions," *Angewandte Chemie International Edition* 64 (2025): e202501190, https://doi.org/10.1002/anie.202501190.

Supporting Information

Additional supporting information can be found online in the Supporting Information section.

Supporting File: anie74831-sup-0001-SuppMat.pdf.

15213773, 2026, 45, Downloaded from https://onlinelibrary.wiley.com/doi/10.1002/anie.4551056 by University Of Science, Wiley Online Library on [02/11/2026]. See the Terms and Conditions (https://onlinelibrary.wiley.com/terms-and-conditions) on Wiley Online Library for rules of use; OA articles are governed by the applicable Creative Commons License